

# Discriminating Seagrasses From Green Macroalgae in European Intertidal areas using high resolution multispectral drone imagery.

Simon Oiry<sup>a,\*</sup>, Bede Ffinian Rowe Davies<sup>a</sup>, Ana I. Sousa<sup>b</sup>, Philippe Rosa<sup>a</sup>, Maria Laura Zoffoli<sup>c</sup>, Guillaume Brunier<sup>d</sup>, Pierre Gernez<sup>a</sup>, Laurent Barillé<sup>a</sup>

<sup>a</sup>*Institut des Substances et Organismes de la Mer, ISOMer, Nantes Université, UR 2160, F-44000 Nantes, France,*

<sup>b</sup>*CESAM – Centre for Environmental and Marine Studies, Department of Biology, University of Aveiro, Aveiro, Portugal,*

<sup>c</sup>*Consiglio Nazionale delle Ricerche, Istituto di Scienze Marine (CNR-ISMAR), 00133 Rome, Italy,*

<sup>d</sup>*BRGM French Geological Survey, Cayenne 97300, French Guiana,*

---

## Abstract

Coastal areas host seagrass meadows, which offer crucial ecosystem services including erosion control and carbon sequestration. However, these areas are increasingly impacted by human activities, leading to seagrass decline and habitat fragmentation. In situ surveys, traditionally performed to monitor these ecosystems face limitations on temporal and spatial coverage, particularly in intertidal zones, prompting the use of satellite data within monitoring programs. Yet, satellite remote sensing struggles with spatial and spectral resolution, making it difficult to discriminate seagrass from other macrophytes in highly heterogenous meadows. To address these challenges, drone images acquired with multi-spectral sensors offer a promising solution. This study focuses on using drones acquisitions for mapping intertidal macrophytes, effectively discriminating between seagrass and green macroalgae. Ten drone flights were conducted at two different altitudes (12m and 120m) across diverse European habitats in France and Portugal. Low altitude flights were used to train a Deep Learning classifier based on Neural Networks to discriminate among 5 intertidal vegetation classes. Drone mapping demonstrated an overall accuracy of 94% across all the sites and images, covering a total area of 467 000 m<sup>2</sup>. The model exhibited an accuracy of 96.4% in identifying seagrass.

*Keywords:* Drone, Remote Sensing

---

\*Corresponding author

Email address: [oirysimon@gmail.com](mailto:oirysimon@gmail.com) (Simon Oiry)

---

## 1. Introduction

Coastal areas are vital hotspots for marine biodiversity, with intertidal seagrass meadows playing a crucial role at the interface between land and ocean [1]. Seagrass meadows provide a myriad of ecosystem services to humanity, including carbon sequestration, oxygen production, protection against sea-level rise and coastline erosion, and limitation of eutrophication. They serve as vital habitats for a diverse array of marine and terrestrial species, providing living, breeding, and feeding grounds [2, ; 3, ; 4]. Due to the concentration of human activities in coastal zones, seagrass meadows are directly exposed to and impacted by anthropogenic pressures. Global regression and fragmentation are currently observed due to climate change, diseases, urbanization, land reclamation, dredging, competition with alien species, and reduction in water quality [5, ; 6, ; 7, ; 8, ; 9]. While improvements in water quality have been recently reported in Europe, allowing an overall recovery of seagrass ecosystems at local scale, many coastal waters worldwide are still subjected to strong eutrophication processes [10, ; 11]. Coastal eutrophication has been associated to anomalous accumulation of green macroalgae, the so-called green tides ([12] ; [12]). Green tides produce shade and suffocation over seagrass individuals, thus threatening the health of seagrass ecosystems [13].

The importance of seagrass meadows and the variety of ecosystem services they provide have led to the enhancement of both global and regional programs monitoring Essential Oceanic Variable (EOVs) such as seagrass composition [14], as well as Essential Biodiversity Variable (EBVs) such as seagrass taxonomic diversity, species distribution, population abundance, and phenology [15]. Seagrass monitoring is all the more important as it makes possible to identify which pressure should be addressed in priority to facilitate effective mitigation actions. Traditionally, indicators of seagrass status have been quantified using in situ measurements. The acquisition of field data in intertidal zones is however notoriously challenging. Intertidal seagrass meadows are only partially exposed during low tide and can be situated in difficult-to-reach mudflats, potentially leading to inaccurate and limited estimations with conventional sampling techniques [16]. Satellite observations have been proven effective in complementing in situ sampling, allowing for the near real-time and consistent retrieval of seagrass EOVs and EBVs over extensive meadows. [11, ; 17, ; 18, ; 19]

While satellite remote sensing provides temporally consistent observations over large spatial scales, it is limited by several constraints. Satellite missions with a high temporal resolution (e.g. daily MODIS observation) are limited by a coarse spatial resolution ( $>100\text{m}$ ). Missions with a high spatial resolution such as Sentinel-2 (10m) or Landsat8/9 (30m) can be limited by low spectral resolution. The limited number of spectral bands is indeed a challenge to accurately discriminate seagrass from others co-existing macrophytes. In particular Chlorophyceae (green algae) and marine Magnoliopsida (seagrass) share the same pig-

ment composition [20, ; 21]. As a result, their respective spectral signatures can be considered similar by a non-expert observer [22, ; 23]. Recently, using advanced machine-learning algorithms trained with a large hyperspectral library of more than 300 field reflectance measurements, [22] demonstrated that it was possible to discriminate Magnoliopsida from Chlorophyceae using radiometric data acquired at Sentinel-2's spectral resolution. The application of this approach to satellite remote sensing remains however to be validated. Moreover patches of green algae can develop at small spatial scales that are not observable using non-commercial satellite imagery [24], especially during the initial stage of the event.

Drone can potentially fill the gaps left by satellite remote sensing and in situ measurements, due to their ability to provide spatially-explicit observations at very high spatial resolutions (pixel size from cm to mm) and still capturing data at multi-spectral resolution [25, ; 26]. The versatility of drones allows for their application across a diverse thematic range, from coastal zone management [27, ; 28, ; 29] to mapping species distribution [30, ; 31, ; 32, ; 33, ; 34]. However, when applied to coastal habitat mapping, most study cases were limited to a single flight, restricting the generalizability of their application over wider geographical scales [33, ; 35, ; 36, ; 34]. The present study aimed at analyzing the potential of multispectral drone remote sensing to map intertidal macrophytes, with a particular focus on discriminating Magnoliopsida and Chlorophyceae. Ten drone flights were performed over soft-bottom intertidal areas along two European countries (France and Portugal), covering a wide range of habitats, from monospecific seagrass meadows to meadows mixed with green or red algae. A deep learning algorithm was trained and validated for macrophyte discrimination, emphasizing applicability across diverse sites without a loss of prediction accuracy.

## 2. Material & Methods

### 2.1. Study sites

Seven study sites distributed between France and Portugal were selected for their relatively extensive intertidal seagrass beds. Two sites are located in Gulf of Morbihan (Figure 1 A), France (47.5791°N, 2.8018°W). This gulf covers an area of 115 km<sup>2</sup> and is only connected to the sea through a 900m wide channel. A total of 53 small islands are scattered across the gulf leading to 250 km of shorelines. Patchy seagrass meadows can be found on a lot of these islands. Within the Gulf of Morbihan we have chosen two sites : one is located in one of these island (Arz island); the other one is located in the southern part of the gulf (Duer). Two others sites are located in Bourgneuf Bay, France (46.9849°N, 2.1488°W). This bay is a semi-enclosed macrotidal bay, protected from waves by Noirmoutier Island. Bourgneuf bay hosts a large intertidal seagrass meadow of about 6 km<sup>2</sup>. Within this meadow, the sites observed by drones (L'Epine and Barbatre, Figure 1 B) contain a monospecific bed of *Zostera noltei* with very little mixing with other macrophytes. Three sites have been surveyed in

the Ria de Aveiro Lagoon in Portugal ( $40.6887^{\circ}\text{N}$ ,  $8.6810^{\circ}\text{W}$ ). The extent of this lagoon is about  $80 \text{ km}^2$  with many narrow channels, large salt marshes and many mudflats that uncovers at low tide. It is connected to the open sea through a single channel, with a tidal lag between the North and the South of the lagoon. The southernmost site (Gafanha) is a mudflat located in an affluent of the lagoon whereas the two other sites are situated in the middle of the lagoon and are only accessible by boat (Figure 1 C). These Portuguese sites are characterized by a more diverse intertidal vegetation, where patches of seagrass could intermingle with red algae (Rhodophyceae), brown algae (Phaeophyceae), and green algae (Chlorophyceae).

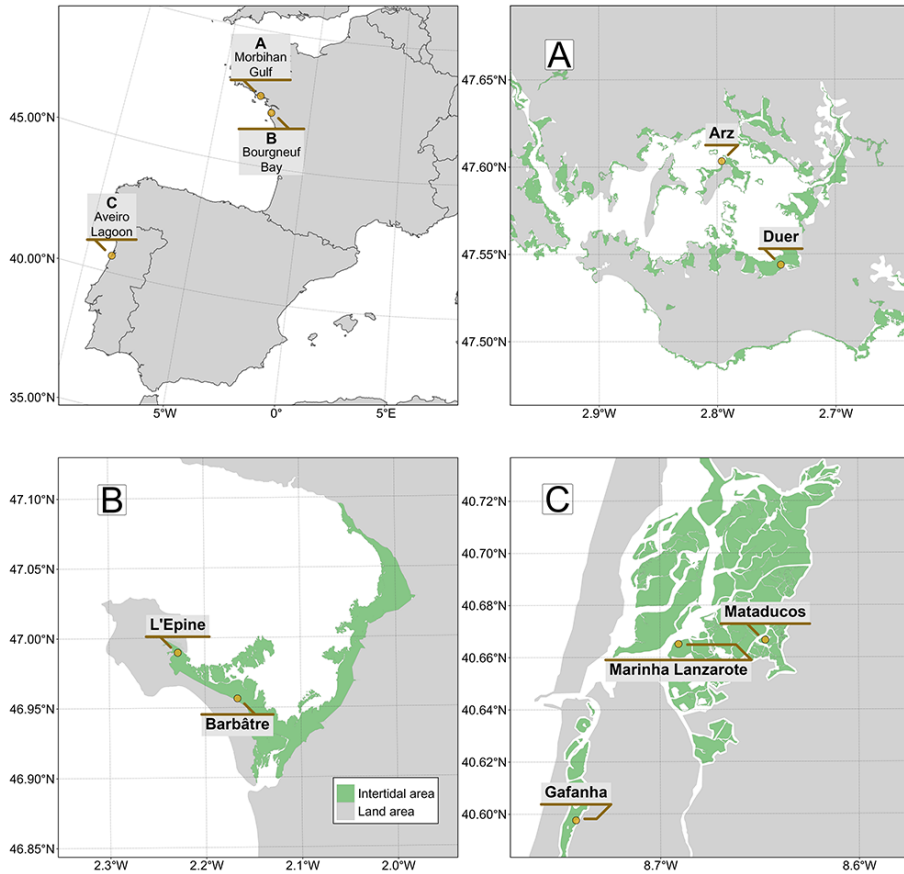


Figure 1: Sites observed by drone. A: Gulf of Morbihan, B: Bourgneuf Bay, C: Ria de Aveiro Lagoon. Light green represent terrestrial areas whereas darkgreen represent intertidal areas.

## 2.2. Drone Data

At each location, a DJI Matrice 200 quadcopter drone equipped with a Micasense RedEdge Dual MX multispectral camera was flown to take 1.2 million pixel reflectance photographs in 10 spectral bands, from 444 nm (blue) to 840 nm (near infrared, NIR). An angle of 90° was maintained between the sun and the drone’s route to guarantee uniform lighting conditions between flight lines. A side overlap of 70% and a front overlap of 80% between each image was set for each flight. A downwelling light sensor (DLS2) was used to acquire irradiance data concomitantly with the camera measurements. Raw data were calibrated in reflectance using a calibration panel reflective at ~50% provided by the manufacturer. A structure-from-motion photogrammetry software (Agisoft Metashape) was used to process images to obtain multispectral orthomosaics of each flight. The workflow for orthomosaicking was the same for every flight. First, tying key points were detected inside of each image and between overlapping images in order to obtain a sparse point cloud. This cloud was cleaned using reprojection accuracy metric in order to remove noisy points. A dense point cloud was then produced using a structure from motion algorithm. A surface interpolation of this dense point cloud was made to obtain a digital surface model (DSM), used to reconstruct the multispectral ortho-image. Across all sites, flights were made at two different altitudes : 12 m or/and 120 m. Low altitude drone flights produce ortho-images with a very high spatial resolution (8 mm per pixel), making it simple to visually distinguish between the various types of vegetation. High altitude flights on the other hand allow to cover large areas and produced images with a pixel size of 80 mm (Table 1).

Table 1: List of drone flight, summarising the date, the altitude and the purpose of each flight.

Country	Site	Name	Altitude	Utility
France	Morbihan	Arz Island	12m	Training
		Duer	12m	Training
	Bourgneuf Bay	Duer	120m	Validation
		Barbâtre	120m	Validation
Portugal	Aveiro Lagoon	L’Epine	120m	Validation
		Inner Lagoon	120m	Validation
		Mataducos	120m	Validation
		Gafanha	120m	Validation
		Gafanha	12m	Training

### 2.3. Field sampling

Before each flight, targets used as Ground Control Points (GCPs) were distributed over the study site and georeferenced with a Trimble © Geo XH 6000 differential GPS (dGPS). GCPs were used to correct georeferencing imprecision of orthomosaics with an horizontal and vertical accuracy of 10cm. dGPS was also used to georeference quadrats of 0.25cm<sup>2</sup> used to assess the presence or absence of 5 key classes of vegetation : Bacillariophyceae (Benthic diatoms forming large biofilm over the sediment during low tide), Phaeophyceae (brown algae), Magnoliopsida (seagrass), Chlorophyceae (green algae) and Rhodophyceae (red algae) (Figure 2). Pictures of each quadrat were uploaded on the online on the Global Biodiversity Information Facility (GBIF) platform [37], a public open portal to store and share biodiversity data. Each photograph was also processed to estimate the percent cover of each type of vegetation using an image processing software (imageJ). For all quadrat, the hyperspectral reflectance signatures of each vegetation class was measured using an ASD FieldSpec HandHeld 2 spectroradiometer, which acquires reflectance between 325 and 1075 nm, with 1 nm of spectral resolution. The methodological scheme followed in this study is presented in Figure 3.

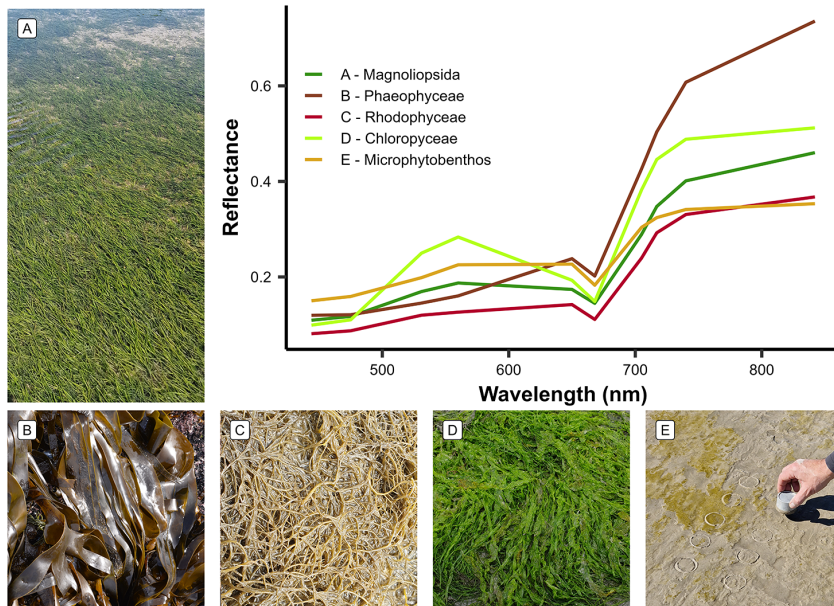


Figure 2: Class of vegetation used to train the Neural Network model and their standardised spectral signature

## 2.4. Intertidal vegetation mapping

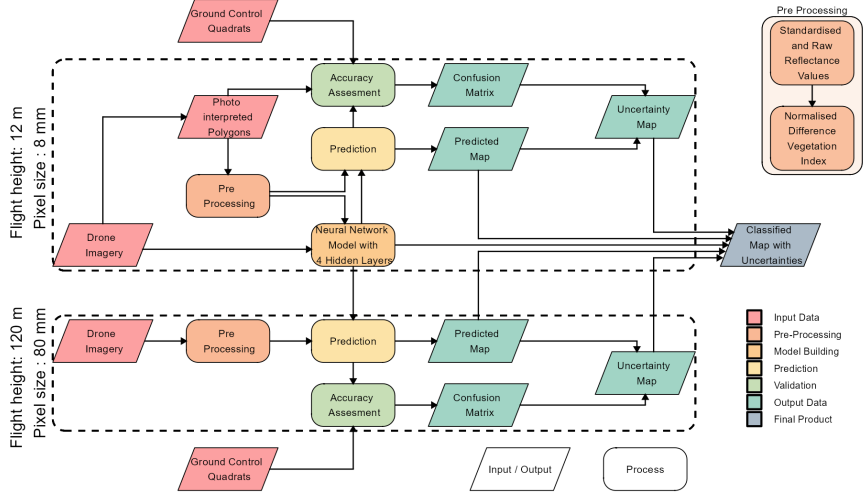


Figure 3: Schematic representation of the workflow. Diamonds represent input or output data, and rectangles represent Python processing algorithms. The overall workflow of this study is divided into two distinct parts based on the spatial resolution of the drone flights: high-resolution flights were utilized for training and prediction of the Neural Network model, whereas low-resolution flights were solely employed for prediction purposes.

The spectral similarities of the reflectance signatures of the intertidal green macrophytes (Magnoliopsida and Chlorophyceae) make their discrimination challenging using simple classification algorithms (Figure 2 F). To overcome this challenge, a deep learning classification method was developed, trained, validated, and applied to each drone flight (Figure 3).

### 2.4.1. Neural Network model building

Table 2: Vegetation Classes of the model and the number of pixels used to train and validate each class

Class	Training Pixels	Validation Pixels
Bacillariophyceae	4,475	3,371,920
Chlorophyceae	17,140	6,258,737
Magnoliopsida	221,065	69,079,189
Phaeophyceae	169,936	18,481,141
Rhodophyceae	5,771	

A dataset containing photo-interpreted drone reflectance pixels was built to train a Neural Network model with 2 hidden layers. The training pixels were categorized into 7 different classes, representing the various habitats encountered at the different study sites: Sediment, Water, Chlorophyceae, Magnoliopsida, Bacillariophyceae, Phaeophyceae and Rhodophyceae. Only low-altitude flights (Table 1) were used for training purposes because their 8 mm spatial resolution allowed to avoid spectral sub-pixel mixing and to accurately differentiate various vegetation classes. More than 418,000 pixels at 8 mm resolution from the 3 training flights were used to train the model (Table 2). Twenty one variables were used by the model as predictors: 10 raw spectral bands of the Micasense RedEdge Dual MX multispectral camera (ranging from 444 nm to 840 nm), the same 10 spectral bands standardized using a min/max transformation (Equation 1 ; [38]) and the Normalized difference vegetation index (NDVI, Equation 2). Standardisation of spectral bands is used to eliminate the scaling differences between spectra and to limit the effect of biomass on the shape of the spectra [21, ; 22].

$$R_i^*(\lambda) = \frac{R_i(\lambda) - \min(R_i)}{\max(R_i) - \min(R_i)} \quad (1)$$

where  $R_i(\lambda)$  is the reflectance at the wavelength ( $\lambda$ ) of each individual spectra ( $i$ ),  $\min(R_i)$ , and  $\max(R_i)$  are the minimum and maximum value of the spectra ( $i$ )

$$NDVI = \frac{R(840nm) - R(668nm)}{R(840nm) + R(668nm)} \quad (2)$$

where  $R(840nm)$  is the reflectance at 840 nm and  $R(668nm)$  is the reflectance at 668 nm.

#### 2.4.2. Validation

The model was applied to all flights at both 12 and 120 m of altitude. In situ information on georeferenced class type and percent cover collected during each flight was used to assess the model accuracy. These images were used to construct a validation dataset indicating the presence or absence of each class. Additionally to the quadrat-based validation dataset, polygons of each class were photo interpreted in order to increase the number of pixels of the validation dataset. A confusion matrix, along with precision metrics such as global accuracy, sensitivity, specificity, and Kappa coefficient, was generated for each sites. All validation matrices were then merged to create a unique matrix . Altogether, a total of 536,000 pixels was used to validate the model, thus providing a geographically robust validation dataset.

### 3. Results

#### 3.1. Classification

A total of 9 prediction maps corresponding to the 9 drone flights were obtained. Each prediction map is associated with a probability map, indicating the probability of the selected class for every pixel. The low-altitude flight conducted in Gafanha, Portugal, represents the site with the highest complexity (Figure 4). Among the 5 vegetation classes on which the model was trained, 4 were present on this site. On this site, there is a mixture of Chlorophyceae and Rhodophyceae over the seagrass meadow. This is also where Bacillariophyceae is most abundant. Although the seagrass bed is solely composed of *Zostera noltei*, various colors can be observed: dark green (indicating healthy beds with 100% coverage) and whitish/brown (indicating beds where leaves are dying). Regardless of the color, the meadow is predicted as Magnoliopsida by the model.

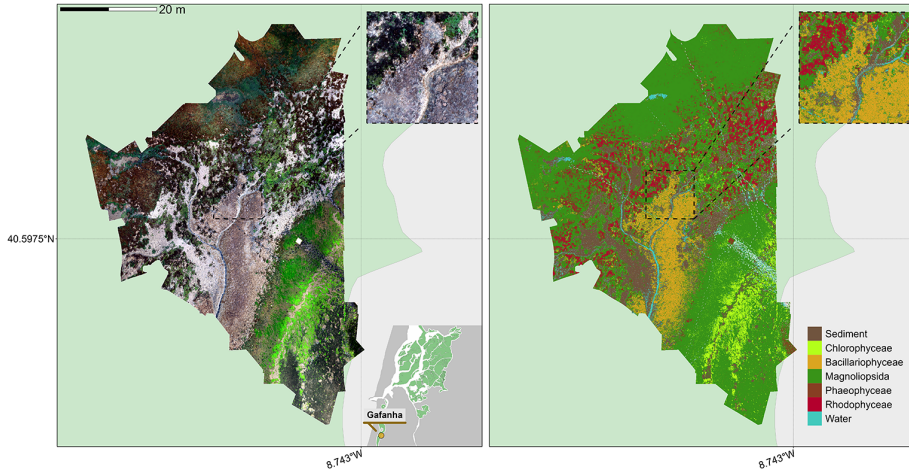


Figure 4: RGB orthomosaic (Left) and Prediction (Right) of the low altitude flight of Gafanha, Portugal. The total extent of this flight is 3000m<sup>2</sup> with a resolution of 8 mm per pixel. Background colors means intertidal area (Light Green) and land area (Light Grey). The zoom covers an area equivalent to a 10-meter Sentinel-2 pixel size.

The high-altitude flight over Gafanha covered nearly 1 km<sup>2</sup> in total (Figure 5). A channel delineating a small island was masked in the prediction map due to sunglint and misclassification caused by the turbid shallow water. Most of the intertidal area has been classified as Magnoliopsida by the model, even though there is discoloration of seagrass blades. Only a few pixels have been classified as Chlorophyceae at this scale. Furthermore, the area that was classified as Bacillariophyceae in the low-altitude flight remains mostly classified as such in the high-altitude flight, though some pixels were classified as Magnoliopsida. Patches of Rhodophyceae were correctly classified. In the northern part of the

scene, near the land limit, patches of *Spartina* sp. were misclassified, either as Magnoliopsida or as Phaeophyceae.

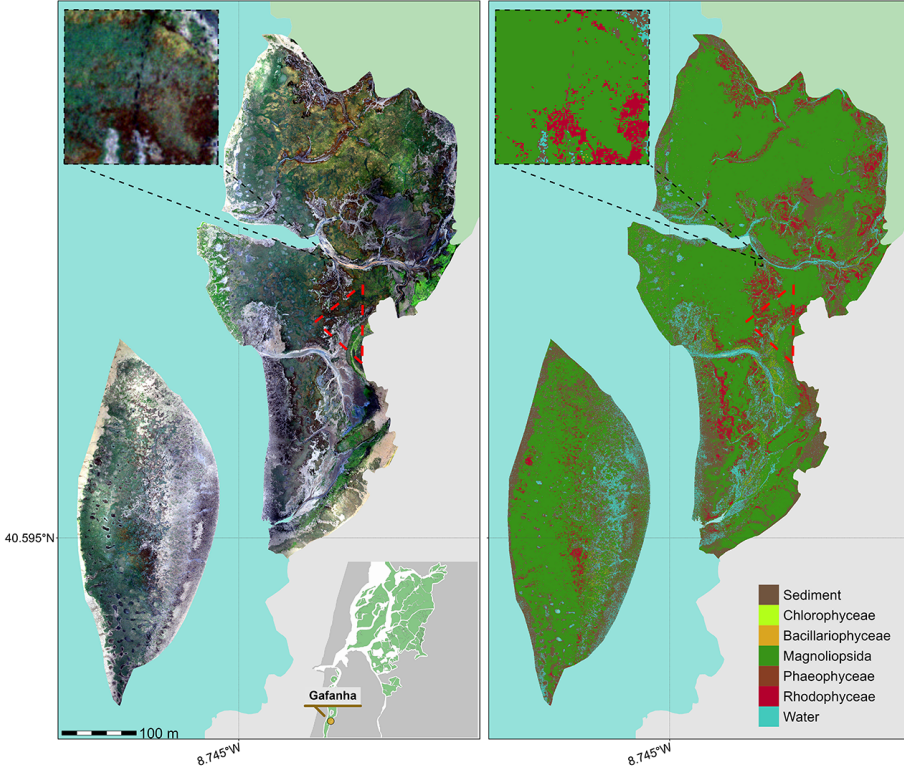


Figure 5: RGB orthomosaic (Left) and Prediction (Right) of the high altitude flight of Gafanha, Portugal. The total extent of this flight is about 1 km<sup>2</sup> with a resolution of 80 mm per pixel. Background colors means intertidal area (Light Green), land area (Light Grey) and water (Light Blue). The red triangle shows the extent of the low altitude flight of Gafanha. The zoom covers an area equivalent to a 10-meter Sentinel-2 pixel size.

The high altitude flight acquired over the inner lagoon of the Ria de Aveiro is the largest of all flights, covering almost 1.5 km<sup>2</sup> (Figure 6). On this site, only seagrass and red algae where seen on the field. The classification provided consistent results, with a patchy Magnoliopsida meadow mixed with Rhodophyceae on the eastern part of the scene. As shown in the zoom (Figure 6), the edges of the meadow can be colonised by Chlorophyceae.

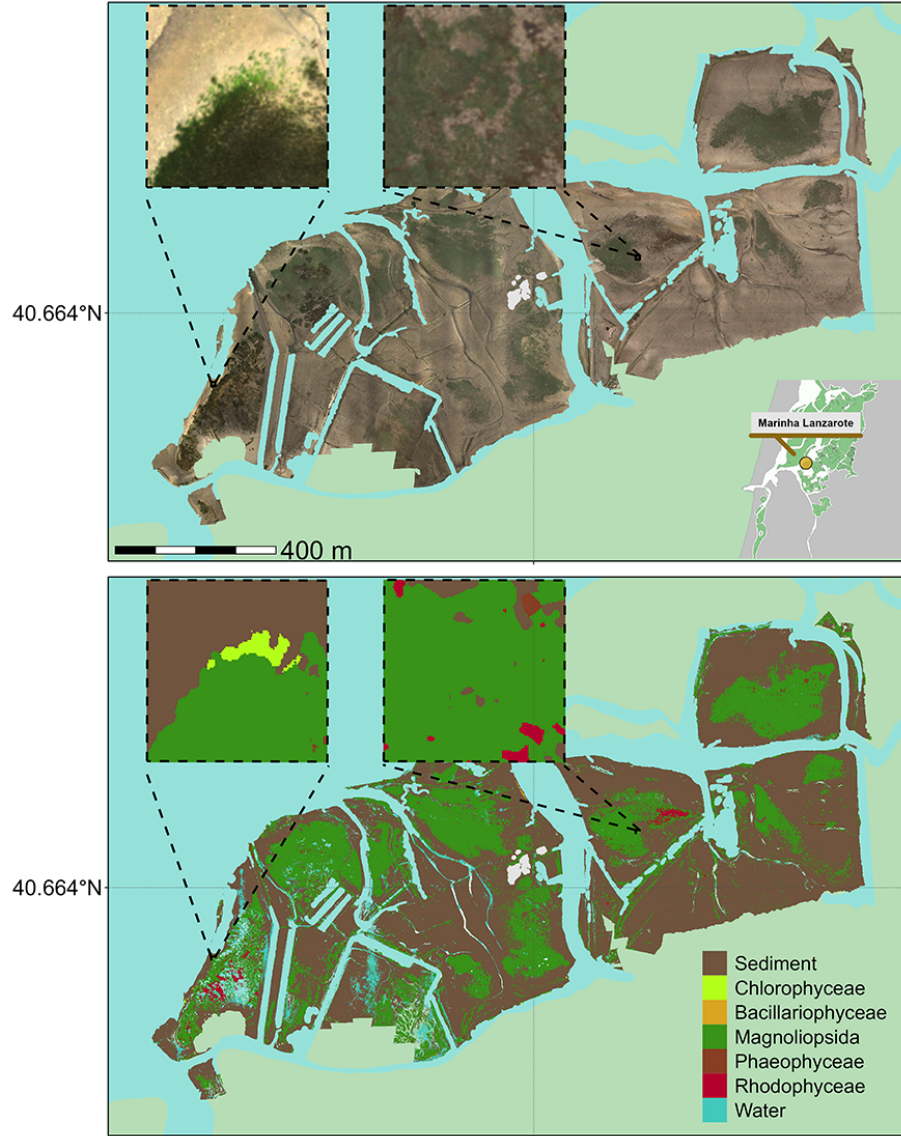


Figure 6: RGB orthomosaic (Top) and Prediction (Bottom) of the flight made in the inner part of Ria de Aveiro Lagoon, Portugal. The total extent of this flight is about 1.5 km<sup>2</sup> with a resolution of 80 mm per pixel. Background colors means intertidal area (Light Green), land area (Light Grey) and water (Light Blue). The zoom covers an area equivalent to a 10-meter Sentinel-2 pixel size.

The flight over L'Epine in Noirmoutier Island, France (Figure 7) was conducted near a dike crossing the northern part of the scene from west to east. Alongside this dike, brown algae attached to rocks and stranded green algae could be found.

Despite the high mixture between Chlorophyceae and Magnoliopsida these two classes were correctly discriminated by the classifier.

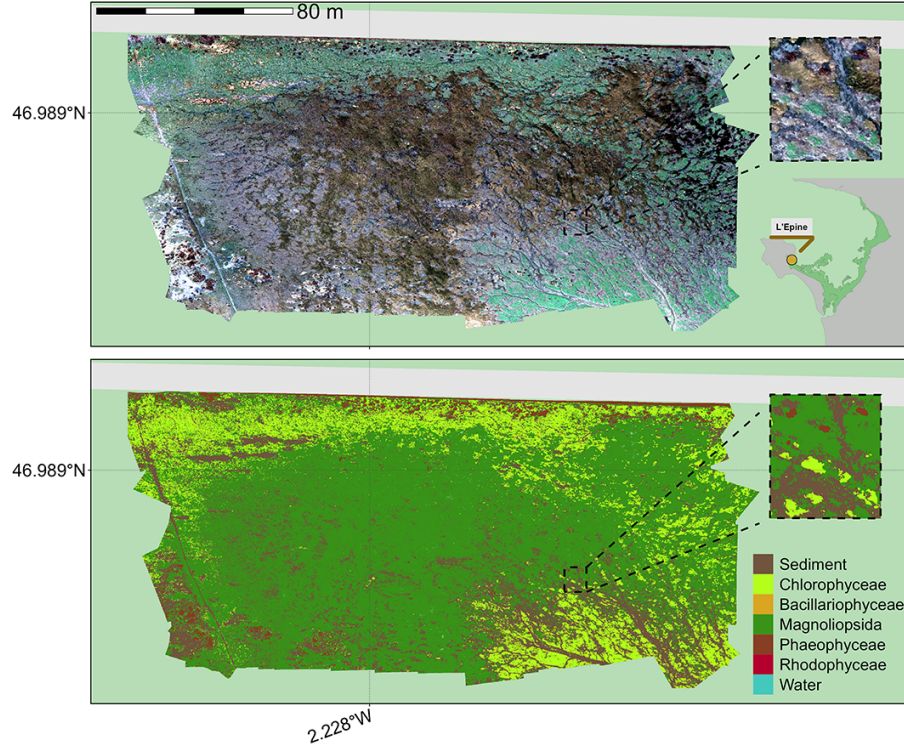


Figure 7: RGB orthomosaic (Top) and Prediction (Bottom) of Northern part of Noirmoutier Island, France. The total extent of this flight is about 28 000 m<sup>2</sup> with a resolution of 80 mm per pixel. Background colors means intertidal area (Light Green) and land area (Light Grey). The zoom covers an area equivalent to a 10-meter Sentinel-2 pixel size.

### 3.2. Validation

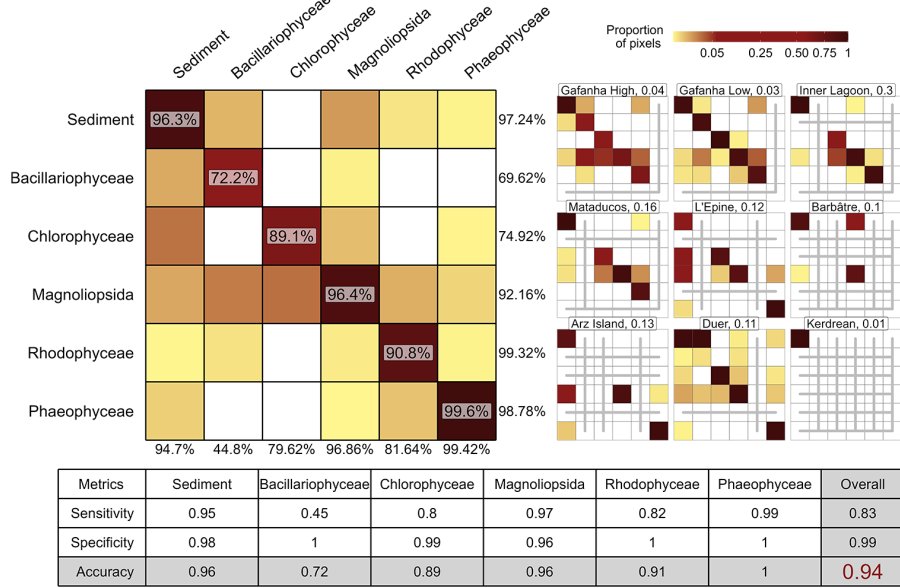


Figure 8: A global confusion matrix on the left is derived from validation data across each flight, while a mosaic of confusion matrices from individual flights is presented on the right. The labels inside the matrices indicate the balanced accuracy for each class. The labels at the bottom of the matrices indicate the User’s accuracy for each class, and those on the right indicate the Producer’s Accuracy. The values adjacent to the names of each site represent the proportion of total pixels from that site contributing to the overall matrix. Grey lines within the mosaic indicate the absence of validation data for the class at that site. The table at the bottom summarizes the Sensitivity, Specificity, and Accuracy for each class and for the overall model.

A total of 536,000 pixels was used to validate the Neural Network classifier. The sites with the lowest and highest number of validation data were Kerdrean (5557 pixels) and Marinha Lanzarote (159713 pixels), respectively. Model global accuracy was 94.26% with a Kappa coefficient of 0.92 (Figure 8). The least performing site was Gafanha High (global accuracy of 75.45%) whereas Mataducos was the site with the most accurate prediction (global accuracy of 98.05%). Overall, the classes Phaeophyceae, Magnoliopsida, Sediment and Rhodophyceae were correctly classified with a balanced accuracy of 1, 0.96, 0.96 and 0.91 respectively. Bacillariophyceae was the least performing class (accuracy of 0.72) mainly due to the confusion between Magnoliopsida and Sediment.

### 3.3. Variable importance

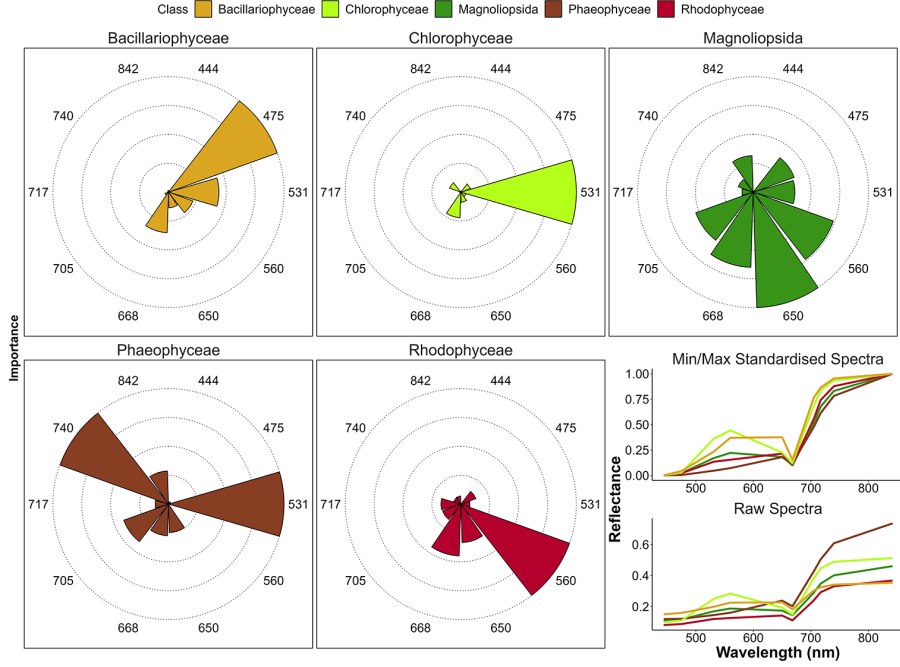


Figure 9: Variable Importance of the Neural Network Classifier for each vegetation class. The bigger the slice, the more important is the variable to predict accurately this class. The bottom right plot shows the drone standardised reflectance spectra of each class.

The computation of the variable importance makes it possible to identify which wavelengths are the most useful for class prediction (Figure 9). The spectral bands at 444 , 717 and 842 nm of the Micasense camera are important for none of the vegetation classes. The band at 531 nm is the only important predictor for the classifier to accurately predict chlorophyceae. In fact, at this wavelength, the Chlorophyceae spectra has the maximum reflectance among of all vegetation classes. The bands at 531 and 740 nm are the most important predictors for Phaeophyceae, corresponding to the minimum reflectance among all classes. Bands at 475 and 560 nm are the most important predictors for Bacillariophyceae and Rhodophyceae, respectively. Four predictors, ranging from the green (560 nm) to the RedEdge (705 nm) bands are important to accurately predict magnoliopsida.

### 3.4. Effect of the flight height on the prediction

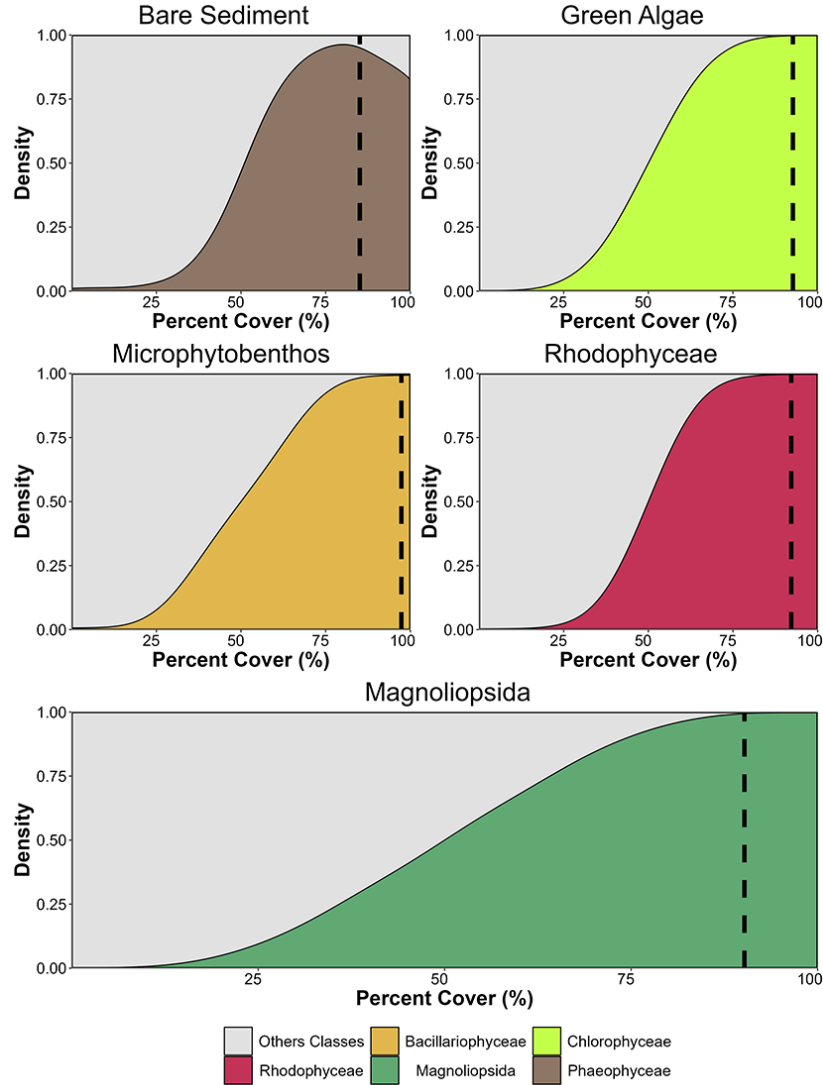


Figure 10: Kernel density plot showing the proportion of pixel well classified based on the percent cover of the class in high altitude flight pixels of Gafanha, Portugal. Each subplot shows all the pixels of the same classes on the hight altitude flight. Percent cover of classes is retrieve using the result of the classification of the low altitude flight of Gafanha, Portugal. The vertical dashed line shows the 0.85 probability of the model. Everything on the right of this line has a probability higher then 0.85 and everuthing on the left of this line has a probability lower.

Using the very high precision low altitude flight, we determined the minimal percent cover required to correctly classify a given class using the high altitude flight (Figure 10). When the percent cover of the class is 100 %, big pixels are well classified for all the classes excepted for Bare Sediment, where it's well classified 80% of the time. A vegetative percent cover of at least 80% is needed to have all the big pixels well classified, at the exception of Magnoliopsida that needs an higher percent cover ( $>90\%$ ) to be well classified. Concerning the probability of each class, a really high Percent cover is needed to confidently predict Bacillariophyceae. To predict Chlorophyceae with a confidence of 0.85, a percent cover of 93 % is needed, 90 % for magnoliopsida, 92 % for Rhodophyceae and 97 % for Bacillariophyceae.

#### 4. Discussion

The primary objective of this study was to develop a method for the accurate classification of macrophytes on intertidal mudflats, specifically focusing on distinguishing between Chlorophyceae (green algae) and marine Magnoliopsida (seagrasses) using multispectral drone data. The challenge arises from the shared pigment composition between these two vegetation classes, complicating their differentiation using remote sensing techniques. This challenge has been addressed through the utilization of high-resolution drone flights allowing a precise photointerpretation of pure pixels of the different vegetation classes used as training data, providing a robust foundation for subsequent classification analyses. In achieving 94.26 accuracy across all study sites, this method demonstrates its efficacy in accurately classifying macrophytes, thus offering a reliable approach for vegetation classification in intertidal mudflats using remote sensing data.

#### 4.1. Vegetation Discrimination

	Chlb	Chlc	Fuco	Zea	Diad	Lut	Neo	PE	PC
Magnoliopsida	Green	Red	Red	Green	Red	Green	Green	Red	Red
Chlorophyceae	Green	Red	Red	Green	Red	Green	Green	Red	Red
Bacillariophy.	Red	Green	Green	Red	Green	Red	Red	Red	Red
Phaeophyceae	Red	Green	Green	Green	Red	Red	Red	Red	Red
Rhodophyceae	Red	Green	Green						
Absorption (nm)	650	636	550	489	496	490	450	566	615

Figure 11: Photosynthetic and carotenoid pigments present (Green) or absent (Red) in each taxonomic class present in the Neural Network Classifier, along with their absorption wavelength measured with spectroradiometer. Chl b: chlorophyll b, Chl c: chlorophyll c, Fuco: fucoxanthin, Zea: zeaxanthin, Diato: diatoxanthin, Diadino: diadinoxanthin, Neo: neoxanthin.

The discrimination of seagrasses from green macroalgae presents significant challenges, primarily due to the shared pigment composition between these taxa, as depicted in Figure 11 but also by the frequent spatial mixing of these green macrophytes. This similarity in pigment composition, including photosynthetic and carotenoid pigments like chlorophyll b and c, fucoxanthin, and neoxanthin, results in spectral signatures that are often indistinguishable to non exper eyes. This spectral overlap is further complicated by the intermingling of seagrasses and green macroalgae in the same spatial locations, posing a significant challenge for remote sensing aimed at accurately mapping and monitoring coastal ecosystems. Our study addresses these complexities by utilizing high-resolution drone imagery with 10 spectral bands. [22] has shown that having at least 8 spectral bands ranging between 500 nm to 850 nm with including a band at 530 nm and another one at 730 nm is crucial to accurately discriminate green macrophytes.

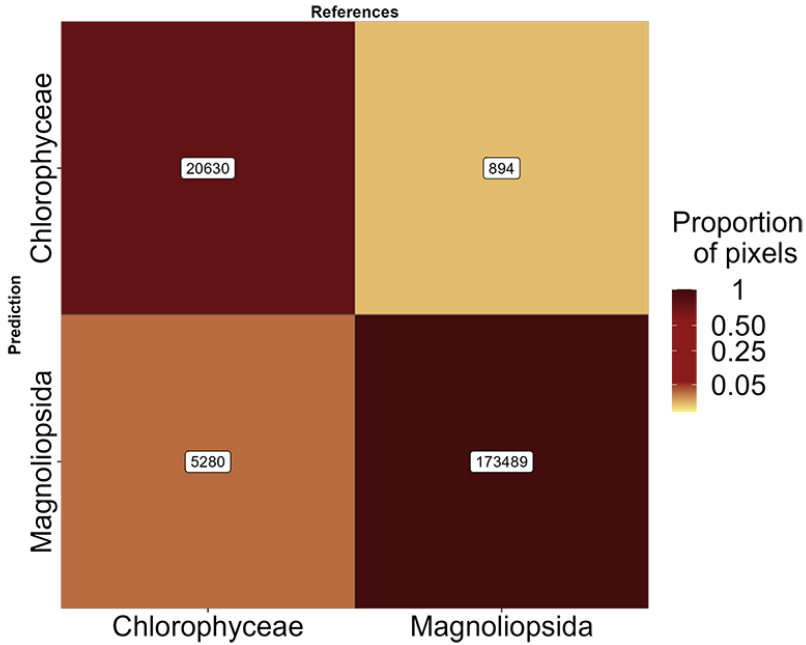


Figure 12: Sample of Figure 8 focusing on green macrophytes. The labels inside the matrice indicate the number of pixels.

The Micasense RedEdge-MX DUAL camera used in this study meets these two criteria, enabling the classifier to achieve 97% of accuracy between these two classes (Figure 12). Even if the pigment composition of green macrophytes is similar, differences in the spectral shape can still be observed (Figure 2). Several factors can explain these differences such as different pigment concentration or proportion, different cellular organisation and 3D disposition of the plant a whole on the intertidal mudflat [39, [40], [41]].

The VIP analysis of the Neural Network model (Figure 9) shows that the 531 nm band is the most important spectral band for accurately identifying Chlorophyceae. In fact, at this wavelength, Chlorophyceae exhibits the highest reflectance among all other classes, highlighting the difference in accessory carotenoid proportion between seagrasses and green algae [42].

Concerning Phaeophyceae, the thick cell walls of plants of this class make it really reflective in the infrared part of the spectra whereas the presence of Fucoxanthin and Zeaxanthin result in a low reflectance in the visible part of the electromagnetic spectra. These two key features have been identified by the Neural Network as the two principal predictors to accurately identify Brown algae (Figure 9). Similarly, the presence of phycoerythrin and phycocyanin in Rhodophyceae contributes to the lowest reflectance among all classes in the spectral range of 560 to 615 nm (Figure 9). The band at 560 nm has been

identified as important for accurately identifying this class Resolution impact on the prediction. Regarding Bacillariophyceae, the VIP analysis (Figure 9) indicates that 475 nm is the most important predictor for this class. This could be attributed to the absence of lutein, neoxanthin, and zeaxanthin in diatoms, absorbing in the blue part of spectra, resulting in the highest visible reflectance among all classes. Furthermore, it is vegetation with the lowest concentration of chlorophyll-a, pigment absorbing light both in the blue and the red. The transparency of Bacillariophyceae makes the reflectance of the sediment part of the overall reflectance of Bacillariophyceae, further explaining the high reflectance in the blue.

#### 4.2. Spectral Spatial Temporal Resolution impact on the prediction

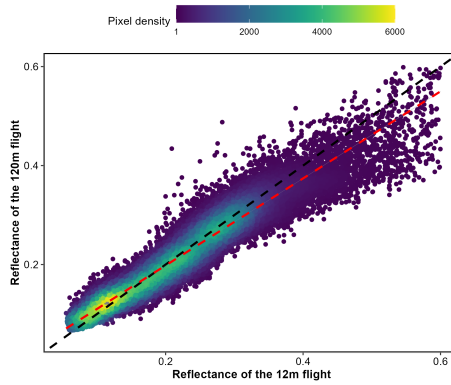


Figure 13: Comparison of reflectance retrieved from both low-altitude and high-altitude flights over a common area. The red dashed line represents a linear model whereas the black dashed line represents a 1 to 1 relationship.

In this study, a key innovation lies in the utilization of two different altitudes (12m and 120m) for constructing the neural network model. The lower altitude flights (8mm spatial resolution) enable precise selection of pure pixels representing the classes used in the neural network model. This methodology implies a consistency between the reflectance of both altitude.

Figure 13 depicts the relationship between reflectance from a low-altitude flight and a high-altitude flight conducted over the same area. An apparent underestimation of reflectance values is observed in the high-altitude flight, particularly for higher values. Since both flights were conducted over vegetation areas, the highest reflectance values correspond to the infrared part of the spectrum. The disparity in infrared reflectance may stem from temporal differences between the flights, possibly resulting in a slightly drier intertidal area and consequently higher infrared reflectance. This disparity poses an issue for the methodology followed in the present study, relying solely on one flight height for training. To address this issue, we employed min/max standardized reflectance spectra

as predictors for the model (Equation 1 ; [38]). This approach allows us to eliminate differences in the level of reflectance, focusing instead on the shape of the spectra. This is a key feature in building a model that can reliably predict vegetation across geographical sites and seasons. It enables consistent prediction of vegetation classes across variations in biomass and variability in light conditions [43, ; 44, ; 45].

#### 4.3. Big picture

### 5. Conclusion

### Bibliography

- [1] R. K. Unsworth, L. C. Cullen-Unsworth, B. L. Jones, R. J. Lilley, The planetary role of seagrass conservation, *Science* 377 (6606) (2022) 609–613.
- [2] R. C. Gardner, C. Finlayson, Global wetland outlook: state of the world's wetlands and their services to people, Stetson Law, 2018.
- [3] M. L. Zoffoli, P. Gernez, S. Oiry, L. Godet, S. Dalloyau, B. F. R. Davies, L. Barillé, Remote sensing in seagrass ecology: coupled dynamics between migratory herbivorous birds and intertidal meadows observed by satellite during four decades, *Remote Sensing in Ecology and Conservation* (12 2022). [doi:10.1002/rse2.319](https://doi.org/10.1002/rse2.319).
- [4] E. Jankowska, L. N. Michel, G. Lepoint, M. Włodarska-Kowalcuk, Stabilizing effects of seagrass meadows on coastal water benthic food webs, *Journal of Experimental Marine Biology and Ecology* 510 (2019) 54–63.
- [5] H. M. Nguyen, P. J. Ralph, L. Marín-Guirao, M. Pernice, G. Procaccini, Seagrasses in an era of ocean warming: a review, *Biological Reviews* 96 (5) (2021) 2009–2030.
- [6] L. M. Soissons, E. P. Haanstra, M. M. Van Katwijk, R. Asmus, I. Auby, L. Barillé, F. G. Brun, P. G. Cardoso, N. Desroy, J. Fournier, et al., Latitudinal patterns in european seagrass carbon reserves: influence of seasonal fluctuations versus short-term stress and disturbance events, *Frontiers in Plant Science* 9 (2018) 88.
- [7] R. J. Orth, T. J. Carruthers, W. C. Dennison, C. M. Duarte, J. W. Fourqurean, K. L. Heck, A. R. Hughes, G. A. Kendrick, W. J. Kenworthy, S. Olyarnik, et al., A global crisis for seagrass ecosystems, *Bioscience* 56 (12) (2006) 987–996.
- [8] H. Lin, T. Sun, Y. Zhou, R. Gu, X. Zhang, W. Yang, Which genes in a typical intertidal seagrass (*Zostera japonica*) indicate copper-, lead-, and cadmium pollution?, *Frontiers in Plant Science* 9 (2018) 1545.

- [9] J. E. Duffy, L. Benedetti-Cecchi, J. Trinanes, F. E. Muller-Karger, R. Ambo-Rappe, C. Boström, A. H. Buschmann, J. Byrnes, R. G. Coles, J. Creed, et al., Toward a coordinated global observing system for seagrasses and marine macroalgae, *Frontiers in Marine Science* 6 (2019) 317.
- [10] C. B. de Los Santos, D. Krause-Jensen, T. Alcoverro, N. Marbà, C. M. Duarte, M. M. Van Katwijk, M. Pérez, J. Romero, J. L. Sánchez-Lizaso, G. Roca, et al., Recent trend reversal for declining european seagrass meadows, *Nature communications* 10 (1) (2019) 3356.
- [11] M. L. Zoffoli, P. Gernez, L. Godet, S. Peters, S. Oiry, L. Barillé, [Decadal increase in the ecological status of a north-atlantic intertidal seagrass meadow observed with multi-mission satellite time-series](#), *Ecological Indicators* 130 (2021) 108033. [doi:10.1016/j.ecolind.2021.108033](https://doi.org/10.1016/j.ecolind.2021.108033).  
URL <https://linkinghub.elsevier.com/retrieve/pii/S1470160X21006981>
- [12] M. Devlin, J. Brodie, Nutrients and eutrophication, in: *Marine Pollution–Monitoring, Management and Mitigation*, Springer, 2023, pp. 75–100.
- [13] Z. Wang, Z. Fang, J. Liang, X. Song, Assessment of global habitat suitability and risk of ocean green tides, *Harmful Algae* 119 (2022) 102324.
- [14] P. Miloslavich, N. J. Bax, S. E. Simmons, E. Klein, W. Appeltans, O. Aburto-Oropeza, M. A. Garcia, S. D. Batten, L. Benedetti-Cecchi, D. M. Checkley, S. Chiba, J. E. Duffy, D. C. Dunn, A. Fischer, J. Gunn, R. Kudela, F. Marsac, F. E. Muller-Karger, D. Obura, Y. J. Shin, [Essential ocean variables for global sustained observations of biodiversity and ecosystem changes](#), *Global Change Biology* 24 (2018) 2416–2433. [doi:10.1111/GCB.14108](https://doi.org/10.1111/GCB.14108).  
URL <https://onlinelibrary.wiley.com/doi/full/10.1111/gcb.14108><https://onlinelibrary.wiley.com/doi/abs/10.1111/gcb.14108><https://onlinelibrary.wiley.com/doi/10.1111/gcb.14108>
- [15] H. M. Pereira, S. Ferrier, M. Walters, G. N. Geller, R. H. Jongman, R. J. Scholes, M. W. Bruford, N. Brummitt, S. H. Butchart, A. Cardoso, et al., Essential biodiversity variables, *Science* 339 (6117) (2013) 277–278.
- [16] W. Nijland, L. Reshitnyk, E. Rubidge, Satellite remote sensing of canopy-forming kelp on a complex coastline: a novel procedure using the landsat image archive, *Remote Sensing of Environment* 220 (2019) 41–50.
- [17] S. Xu, S. Xu, Y. Zhou, S. Yue, X. Zhang, R. Gu, Y. Zhang, Y. Qiao, M. Liu, Long-term changes in the unique and largest seagrass meadows in the bohai sea (china) using satellite (1974–2019) and sonar data: Implication for conservation and restoration, *Remote Sensing* 13 (5) (2021) 856.
- [18] D. Traganos, P. Reinartz, Mapping mediterranean seagrasses with sentinel-2 imagery, *Marine Pollution Bulletin* 134 (2018) 197–209. [doi:10.1016/j.marpolbul.2017.06.075](https://doi.org/10.1016/j.marpolbul.2017.06.075).

- [19] M. M. Coffey, D. D. Graybill, P. J. Whitman, B. A. Schaeffer, W. B. Salls, R. C. Zimmerman, V. Hill, M. C. Lebrasse, J. Li, D. J. Keith, et al., Providing a framework for seagrass mapping in united states coastal ecosystems using high spatial resolution satellite imagery, *Journal of Environmental Management* 337 (2023) 117669.
- [20] P. Ralph, S. Polk, K. Moore, R. Orth, W. Smith Jr, Operation of the xanthophyll cycle in the seagrass *zostera marina* in response to variable irradiance, *Journal of Experimental Marine Biology and Ecology* 271 (2) (2002) 189–207.
- [21] F. Douay, C. Verpoorter, G. Duong, N. Spilmont, F. Gevaert, [New hyperspectral procedure to discriminate intertidal macroalgae](#), *Remote Sensing* 14 (2) (2022). [doi:10.3390/rs14020346](https://doi.org/10.3390/rs14020346).  
URL <https://www.mdpi.com/2072-4292/14/2/346>
- [22] B. F. R. Davies, P. Gernez, A. Geraud, S. Oiry, P. Rosa, M. L. Zofoli, L. Barillé, [Multi- and hyperspectral classification of soft-bottom intertidal vegetation using a spectral library for coastal biodiversity remote sensing](#), *Remote Sensing of Environment* 290 (2023) 113554. [doi:10.1016/j.rse.2023.113554](https://doi.org/10.1016/j.rse.2023.113554).  
URL <https://www.sciencedirect.com/science/article/pii/S0034425723001050>
- [23] A. Bannari, T. S. Ali, A. Abahussain, The capabilities of sentinel-msi (2a/2b) and landsat-oli (8/9) in seagrass and algae species differentiation using spectral reflectance, *Ocean Science* 18 (2) (2022) 361–388.
- [24] F. Tuya, H. Hernandez-Zerpa, F. Espino, R. Haroun, Drastic decadal decline of the seagrass *cymodocea nodosa* at gran canaria (eastern atlantic): interactions with the green algae *caulerpa prolifera*, *Aquatic Botany* 105 (2013) 1–6.
- [25] I. Fairley, B. J. Williamson, J. McIlvenny, N. King, I. Masters, M. Lewis, S. Neill, D. Glasby, D. Coles, B. Powell, et al., Drone-based large-scale particle image velocimetry applied to tidal stream energy resource assessment, *Renewable Energy* 196 (2022) 839–855.
- [26] J. Oh, D.-j. Kim, H. Lee, Use of a drone for mapping and time series image acquisition of tidal zones, *Journal of the Korean Institute of Intelligent Systems* 27 (2) (2017) 119–125.
- [27] R. Adade, A. M. Aibinu, B. Ekumah, J. Asaana, Unmanned aerial vehicle (uav) applications in coastal zone management—a review, *Environmental Monitoring and Assessment* 193 (2021) 1–12.
- [28] E. Casella, J. Drechsel, C. Winter, M. Benninghoff, A. Rovere, Accuracy of sand beach topography surveying by drones and photogrammetry, *Geo-Marine Letters* 40 (2020) 255–268.

- [29] D. B. Angnuureng, K. Brempong, P. Jayson-Quashigah, O. Dada, S. Akuoko, J. Frimpomaa, P. Mattah, R. Almar, Satellite, drone and video camera multi-platform monitoring of coastal erosion at an engineered pocket beach: A showcase for coastal management at elmina bay, ghana (west africa), *Regional Studies in Marine Science* 53 (2022) 102437.
- [30] K. E. Joyce, K. C. Fickas, M. Kalamandeen, The unique value proposition for using drones to map coastal ecosystems, *Cambridge Prisms: Coastal Futures* 1 (2023) e6.
- [31] K. Tallam, N. Nguyen, J. Ventura, A. Fricker, S. Calhoun, J. O'Leary, M. Fitzgibbons, I. Robbins, R. K. Walter, Application of deep learning for classification of intertidal eelgrass from drone-acquired imagery, *Remote Sensing* 15 (9) (2023) 2321.
- [32] M. Roca, M. B. Dunbar, A. Román, I. Caballero, M. L. Zoffoli, P. Gernez, G. Navarro, Monitoring the marine invasive alien species rugulopteryx okamurae using unmanned aerial vehicles and satellites, *Frontiers in Marine Science* 9 (10 2022). [doi:10.3389/fmars.2022.1004012](https://doi.org/10.3389/fmars.2022.1004012).
- [33] A. Román, A. Tovar-Sánchez, I. Olivé, G. Navarro, Using a uav-mounted multispectral camera for the monitoring of marine macrophytes, *Frontiers in Marine Science* (2021) 1225.
- [34] G. Brunier, S. Oiry, Y. Gruet, S. F. Dubois, L. Barillé, [Topographic analysis of intertidal polychaete reefs \(\*sabellaria alveolata\*\) at a very high spatial resolution](#), *Remote Sensing* 2022, Vol. 14, Page 307 14 (2022) 307. [doi:10.3390/RS14020307](https://doi.org/10.3390/RS14020307).  
URL <https://www.mdpi.com/2072-4292/14/2/307>
- [35] A. Collin, S. Dubois, D. James, T. Houet, Improving intertidal reef mapping using uav surface, red edge, and near-infrared data, *Drones* 3 (3) (2019) 67.
- [36] T. Rossiter, T. Furey, T. McCarthy, D. B. Stengel, Uav-mounted hyperspectral mapping of intertidal macroalgae, *Estuarine, Coastal and Shelf Science* 242 (2020) 106789.
- [37] B. F. R. Davies, A. I. Sousa, R. Figueira, S. Oiry, P. Gernez, L. Barillé, Benthic intertidal vegetation from the tagus estuary and aveiro lagoon (2023). [doi:10.15468/n4ak6x](https://doi.org/10.15468/n4ak6x).
- [38] J. Cao, J. T. Thorson, R. A. Richards, Y. Chen, Spatiotemporal index standardization improves the stock assessment of northern shrimp in the gulf of maine, *Canadian Journal of Fisheries and Aquatic Sciences* 74 (2017) 1781–1793. [doi:10.1139/cjfas-2016-0137](https://doi.org/10.1139/cjfas-2016-0137).
- [39] K. Beach, H. Borgeas, N. Nishimura, C. Smith, In vivo absorbance spectra and the ecophysiology of reef macroalgae, *Coral Reefs* 16 (1997) 21–28.

- [40] J. T. Kirk, Light and photosynthesis in aquatic ecosystems, Cambridge university press, 1994.
- [41] J. D. Hedley, M. Mirhakak, A. Wentworth, H. M. Dierssen, Influence of three-dimensional coral structures on hyperspectral benthic reflectance and water-leaving reflectance, *Applied Sciences* 8 (12) (2018) 2688.
- [42] T. Repolho, B. Duarte, G. Dionísio, J. R. Paula, A. R. Lopes, I. C. Rosa, T. F. Grilo, I. Caçador, R. Calado, R. Rosa, Seagrass ecophysiological performance under ocean warming and acidification, *Scientific Reports* 7 (1) (2017) 41443.
- [43] S. Fyfe, Spatial and temporal variation in spectral reflectance: Are seagrass species spectrally distinct?, *Limnology and Oceanography* 48 (1part2) (2003) 464–479.
- [44] V. Costa, J. Serôdio, A. I. Lillebø, A. I. Sousa, Use of hyperspectral reflectance to non-destructively estimate seagrass *zostera noltei* biomass, *Ecological Indicators* 121 (2021) 107018.  
*doi:*<https://doi.org/10.1016/j.ecolind.2020.107018>.  
URL <https://www.sciencedirect.com/science/article/pii/S1470160X20309572>
- [45] E. Piaser, A. Berton, R. Bolpagni, M. Caccia, M. B. Castellani, A. Coppi, A. Dalla Vecchia, F. Gallivanone, G. Sona, P. Villa, Impact of radiometric variability on ultra-high resolution hyperspectral imagery over aquatic vegetation: preliminary results, *IEEE Journal of Selected Topics in Applied Earth Observations and Remote Sensing* (2023).